Soft Matter

PAPER

View Article Online
View Journal | View Issue

Cite this: *Soft Matter*, 2015, **11**, 5872

The role of curvature anisotropy in the ordering of spheres on an ellipsoid

Christopher J. Burke,[a] Badel L. Mbanga,[a] Zengyi Wei,[b] Patrick T. Spicer[b] and Timothy J. Atherton*[a]

Received 8th May 2015,
Accepted 16th June 2015

DOI: 10.1039/c5sm01118c

www.rsc.org/softmatter

Non-spherical emulsion droplets can be stabilized by densely packed colloidal particles adsorbed at their surface. In order to understand the microstructure of these surface packings, the ordering of hard spheres on ellipsoidal surfaces is determined through large scale computer simulations. Defects in the packing are shown generically to occur most often in regions of strong curvature; however, the relationship between defects and curvature is nontrivial, and the distribution of defects shows secondary maxima for ellipsoids of sufficiently high aspect ratio. As with packings on spherical surfaces, additional defects beyond those required by topology are observed as chains or "scars". The transition point, however, is found to be softened by the anisotropic curvature which also partially orients the scars. A rich library of symmetric commensurate packings are identified for low particle number. We verify experimentally that ellipsoidal droplets of varying aspect ratio can be arrested by surface-adsorbed colloids.

1 Introduction

Emulsions—mixtures of two immiscible fluids—are ubiquitous systems with many applications in the food, oil, and cosmetics industries. At the microscopic level, an emulsion consists of droplets of one fluid embedded in a host fluid; the droplets are held in an equilibrium spherical shape by the interfacial tension between the two fluids. Emulsions with anisotropic droplets are of interest because for some applications, *e.g.* particle filtering in porous media,[1] performance is improved with increasing aspect ratio. Anisotropic particles are also known to be more easily absorbed by cells, thus being effective as drug delivery systems.[2,3] Additionally, ellipsoids fill space more efficiently than spheres,[4] and through chemical functionalization, are a valuable component in the nano-architecture of hierarchical structures.[5]

A mechanism for sculpting stable shaped droplets exists in Pickering emulsions, where the constituent droplets are stabilized by colloidal particles adsorbed at the interface.[6] The particles are strongly bound to the surface because they reduce the interfacial tension between the two immiscible phases.[7] Non-spherical shapes can be produced by a sequence of deformation, adsorption, relaxation and arrest as follows: an initial deformation is applied, for example by an applied electric field[8] or by the coalescence of two droplets;[9] during this process additional particles may become adsorbed on the interface from the host fluid. The droplet then relaxes towards the equilibrium spherical shape, reducing the surface area and causing the particles to become more densely packed. If the surface coverage of colloids is sufficiently high, they will become crowded and arrest the shape evolution of the droplet before a spherical shape is reached.[9,10]

The purpose of this paper is to identify the role that the anisotropic curvature present in an ellipsoid plays on the ordering of the particles. We assume the particles interact purely through volume exclusion. The quality of the packing of the final state, measured globally by coverage fraction as well as locally by coordination number, depends on the ratio of the relaxation timescale τ_r to the particle diffusion timescale τ_d. As $\tau_r/\tau_d \to 0$, the particles are unable to rearrange themselves significantly and may get trapped in a glassy state, while for $\tau_r/\tau_d \to \infty$, the relaxation proceeds slowly and the situation resembles a classical sphere packing problem. It is this latter quasi-static limit of the relaxation process that we shall examine in this work.

Since the colloids are confined to a 2D surface, the arrested states tend to be quite crystalline as has been shown for spherical droplets or *colloidosomes*.[11] These structures should, therefore, exhibit properties similar to 2D elastic crystalline membranes.[12–22] The presence of curvature frustrates the crystalline order and induces defects: particles which have more or fewer than six neighbors, and whose deviation from six-fold order can be quantified as a topological charge: particles with coordination number lower than six have positive charge

[a] *Tufts University, Department of Physics and Astronomy, Center for Nanoscopic Physics, 5 Colby Street, Medford, Massachusetts 02155, USA. E-mail: timothy.atherton@tufts.edu*
[b] *UNSW Australia, Department of Chemical Engineering, Chemical Sciences Building, Gate 2 High Street, Kensington, NSW 2052, Australia*

and *vice versa*. Lone defects of positive or negative charge are known as disclinations. The topology of the droplet surface will determine the net defect charge, which is 12 for a spherical topology.[23] Furthermore, there is a coupling of defects to the Gaussian curvature K. Because droplets with non-spherical geometries possess a variation in Gaussian curvature along their surface, the defects should be non-uniformly distributed as theoretical studies have predicted.[18–20]

In addition to the minimal number of defects required by topology, pairs of positive and negative defects called dislocations can occur. Droplets with a large system size, *i.e.* where the ratio R/r of the droplet size R to the particle size r is large enough, exhibit chains of defects known as scars.[14,16] For spherical droplets, a transition has been shown: if R/r is below a critical value only isolated defects occur. Above this ratio, scars appear and increase in length with R/r.[16]

For surfaces of nonuniform curvature, the placement of the defects is an interesting question. The theory of curved elastic crystalline membranes[14] predicts that defects and Gaussian curvature act as source terms in a biharmonic equation,

$$\nabla^4\chi(\vec{x}) = \rho(\vec{x}) - K(\vec{x}), \quad (1)$$

where χ is a stress function and ρ is the defect charge density (a sum of point charges). The energy of such a system is,

$$U = \int_S \mathrm{d}A\chi(\vec{x})(\rho(\vec{x}) - K(\vec{x})), \quad (2)$$

which must be minimized with respect to defect number and defect position, with total defect charge conserved according to the surface topology. While this suggests that defect charges will be attracted to areas of like-signed curvature in order to minimize the source term, the fact that these systems are governed by a biharmonic equation suggests that the coupling of defects to curvature is nontrivial. This is in contrast to simpler analogues, for example electrostatics, governed by a Poisson equation.

There are two important differences between an elastic crystalline membrane and a 2D arrested hard sphere system. First, in the hard sphere limit, the in-plane elastic constants of a hard sphere system are infinite. Second, arrested hard sphere systems are not able to explore their full phase space, and as such belong to a class of systems with arrested kinetics that is not fully understood.[24] It is therefore unclear whether energy optimization principles can be invoked for the ensemble of arrested states generated by the model used in this paper. One of the aims of this paper is to clarify the relationship between arrested hard sphere systems and optimal energy models. Additionally, the relative wetting properties of the two fluids may induce a contact angle, leading to inter-particle interactions that may modify the ordering.[25]

In other systems in the packing limit, *e.g.* viral capsids[26] and small clusters of colloids,[27] configurations with a high degree of symmetry are typically observed for certain special numbers of particles. Experimentally, these tend to be stable, and so the identification of possible symmetric packings may serve as a guide towards stable self-assembled micro-structures.

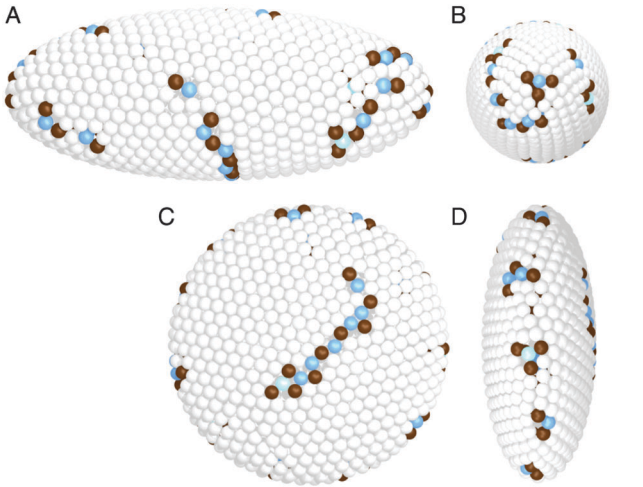

Fig. 1 Sample packing of N = 800 particles on a prolate ellipsoid of aspect ratio 2.6. (A) Side and (B) end views are shown; corresponding plots are shown for an oblate ellipsoid of aspect ratio 2.6 (C) from the top and (D) around the rim. Particles are colored by coordination number as computed from the Delaunay triangulation of the centroids — 5: brown; 6: white; 7: blue; 8: light blue.

We therefore examine the packings systematically by aspect ratio a and particle number N to identify the symmetric configurations.

In order to explore the role of surface anisotropy on the ordering of packed particles, we present the results of simulations of hard spheres packed onto ellipsoidal surfaces using an inflation algorithm. Sample results are shown in Fig. 1. We investigate the effect of aspect ratio and particle number on the average distribution of defects on our surfaces and the structure of the defects themselves. We also identify highly symmetric configurations. Experimentally, we demonstrate that ellipsoidal droplets can be stabilized by surface-adsorbed colloids, and we compare the spatial distribution of defects in the experiments and simulations. Details of the model and simulations are presented in Methods.

2 Results and discussion

We employ an inflation packing algorithm in order to generate packings of spheres on ellipsoidal surfaces. The centroids of N equal sized spheres are bound to a fixed ellipsoidal surface, either prolate or oblate, of aspect ratio a. The particles have hard-sphere interactions and diffuse as the particle radius is slowly incremented, until further inflation is precluded. Further details of the algorithm are given in Methods.

Two sets of data were generated from which we obtained our results. One data set was used for studying the curvature-defect coupling and scar length, which consisted of packings with aspect ratio varying from 1.2 to 4.0 in increments of 0.2 (for both the prolate and oblate cases: we consider the aspect ratio to be the ratio of the semi-major to semi-minor axis.) The particle number was varied from 10 to 800 in increments of 10. Additional prolate packings were generated to study scar orientation, from aspect ratio 4.2 to 8.0 in increments of 0.2, from

particle number 710 to 800 in increments of 10. 50 configurations were generated for each pair of parameters. The second data set was used for studying symmetry, where we are interested in lower particle numbers and a more fine-grained search of the parameter space. This data set consisted of packings with aspect ratio varying from 1.1 to 4.0 in increments of 0.1, and particle number varying from 3 to 200 in increments of unity. 80 configurations were generated for each pair of parameters.

2.1 Defect distribution

We first examined the distribution of the defects as a function of the aspect ratio. Defect locations were determined by assigning a defect charge $q = 6 - c$ to each particle, where c was the coordination number determined from the Delaunay triangulation of the particle positions (see Methods). The surface was partitioned into equal-area axisymmetric regions and the number of defects in each region counted. Each segment has a different average Gaussian curvature with regions near the poles having larger curvature for prolate and the reverse for oblate ellipsoids. In Fig. 2A for prolates and Fig. 2B for oblates, the defect number density is shown as a function of the axial position z/z_0 averaged over the ensemble of simulations at fixed aspect ratio and particle numbers ranging from $710 < N < 800$. Generically, it is apparent that defect number density increases with the Gaussian curvature, as expected. For prolate ellipsoids at low aspect ratio, the defect number density increases monotonically with respect to K. At higher aspect ratios, there is a small secondary peak in segments with low Gaussian curvature. We verified this occurs for other ranges of particle numbers $N > 210$.

In order to understand this, we plot separate defect charge densities for positive and negative defects in Fig. 2C, as well as the net defect charge density. The anomalous peak is apparent in both the separate positive and negative defect charge densities, but not in the net defect charge density, indicating that the excess defects are taking the form of neutral dislocations or scars.

In Fig. 2B, we see that for oblate ellipsoids, the defect density again increases near the more highly curved regions. Fig. 2D reveals, however, that the coupling between defect charge and curvature is again complicated: while there is a peak in positive defects at the highly positively curved edge of the surface, there is a high density of negative defects surrounding this, and the net defect charge density is actually negative near $z/z_0 = 0.4$.

Previous studies[21] have shown that the defect charge present on a curved surface is determined by the integrated Gaussian curvature of that surface, such that

$$\frac{1}{\pi/3}\int K \mathrm{d}A = \sum_{i=1}^{n} q_i. \qquad (3)$$

To test whether this model is consistent with our results, we plot the integrated curvature, normalized as in eqn (3), in each of the equal-area segments described above, and compare this with the net defect charge in those sections. The results for prolate ellipsoids of different aspect ratios are shown in Fig. 2E as dashed lines, and there is excellent agreement between the model and the simulation data. The result for oblate ellipsoids, shown in Fig. 2F, do not show agreement. This is unsurprising, given the negative net defect charge present in the simulation results.

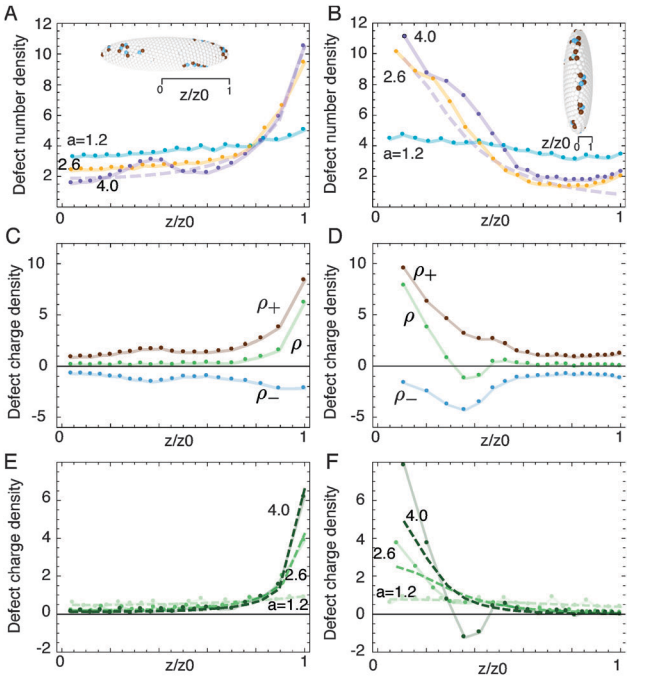

Fig. 2 Defect number density for (A) prolate and (B) oblate ellipsoids of varying aspect ratio: blue is 1.2; yellow 2.6; purple 4.0. Points with solid lines represent simulation data. Dashed lines represent the prediction of the model in eqn (4) for surfaces of aspect ratio 4.0. Note the small secondary peak near $z/z_0 = 0.4$ at $a = 4$ in the prolate case. Example configurations of $a = 4$ are shown as insets. Defect charge density is shown for (C) prolate and (D) oblate ellipsoids of $a = 4$. The green points represent the net charge density, and the brown and blue points represent the density of positive and negative defects, respectively. The secondary peak in (A) is also visible in the positive and negative charge densities in (C). In (D), there is a net negative defect charge density near $z/z_0 = 0.4$, despite the Gaussian curvature being positive. Net defect charge densities for different aspect ratios are compared to the integrated Gaussian curvature (dashed lines) for (E) prolate and (F) oblate ellipsoids. In all plots, densities are given in units of defect number or defect charge per equal-area segment, averaged over the ensemble of simulation results, with symmetric segments on opposite halves of a surface being combined. Lines are guides to the eye.

This model can be extended to attempt to account for excess dislocations which occur in addition to the topologically required core disclinations. As will be discussed further in the scar transition subsection below, excess dislocations appear in the form of scars in packings of particles on spherical surfaces when R/r, the ratio of surface radius to particle radius, is above a critical value, and above this value the scar length grows linearly with R/r;[14,16] other work similarly suggests that the stability of scars depends on the ratio of the particle size to the lateral size of the inter-disclination domain.[21,28] On a non-spherical surface such as an ellipsoid, there is not a single surface radius R,

but one can estimate a local surface radius based on the Gaussian curvature as $1/\sqrt{K}$. One can then assume that for each core disclination (whose surface density is predicted by K), there is a scar made up of some number of dislocations n_s given by $1/(r\sqrt{K})$. We fit the scar length data for hard particles packed on spheres from Fig. 5 to get a function $n_s(R/r)$ and use this to model the defect number density ρ_n as,

$$\rho_n = \frac{K}{\pi/3}\left(1 + 2n_s\left(\frac{1}{r\sqrt{K}}\right)\right). \quad (4)$$

This model at first glance seems like a promising candidate to explain the non-monotonic nature of the observed defect distributions on prolate ellipsoids, as there is a competition between high disclination density and low scar length in regions of high K, and low disclination density and high scar length in regions of low K. Upon calculating the defect density, shown in Fig. 2A, we see that, while this model accurately predicts the magnitude of the defect number density across much of the surface for prolate ellipsoids, it fails to capture the anomolous bump. The model does not accurately predict the defect number density for oblate ellipsoids; it underpredicts it across the entire surface (Fig. 2B).

These results display a non-trivial interaction between defects and curvature. While the regions of highest Gaussian curvature contain the highest density of defects, the defect density is not a simple monotonic function of Gaussian curvature. This is apparent in the defect number density in the prolate case, and in the defect charge density in the oblate case. The fact that the defect charge density can be negative in regions of positive Gaussian curvature is especially surprising. However, this is not necessarily inconsistent with eqn (1) and (2), which imply complex defect behavior. Further investigation is warranted to confirm whether the continuum elastic theory gives results similar to the hard sphere packings here.

2.2 Scar orientation

We next determined whether the scars are oriented by the curvature anisotropy of the surface. To do so, we consider a local scar orientational distribution function (ODF) $f(\alpha)$ where the angle α is measured locally in the tangent plane relative to the uniaxial axis of the ellipsoid. The ODF may be expanded as a Fourier series,

$$f(\alpha) = \sum_n C_n \cos(n\alpha). \quad (5)$$

The average value of the first two non-zero coefficients, $C_2 = \langle\cos(2\alpha)\rangle$ and $C_4 = \langle\cos(4\alpha)\rangle$, were calculated for our ensemble of packings. These quantities are order parameters for orientational order as they vanish if the scars align isotropically with the curvature. C_2 quantifies nematic order, *i.e.* uniaxial orientational order and C_4 quantifies quadrupolar order.

To determine the scar orientation, we studied contiguous chains of defects as shown in Fig. 3A and B. Given a packing and its Delaunay triangulation, the neighboring defects around each defect are identified. These adjacent pairs become the edges of graphs of contiguous defects. Two defects are identified as the ends of a chain of length l if they are within a connected graph of defects and the shortest path between them contains l edges. Once a chain of length l is identified, its orientation relative to the local principal directions— *i.e.* the polar and azimuthal tangent vectors $\vec{t}_\theta$ and $\vec{t}_\phi$, respectively (see eqn (10) in the Appendix for the parametrization of the surface)— is calculated thus: given a pair of chain endpoints, their separation vector is projected onto the surface at each endpoint, giving components along $\vec{t}_\theta$ and $\vec{t}_\phi$. These components are then averaged between the endpoints, and the angle α that the resulting vector makes

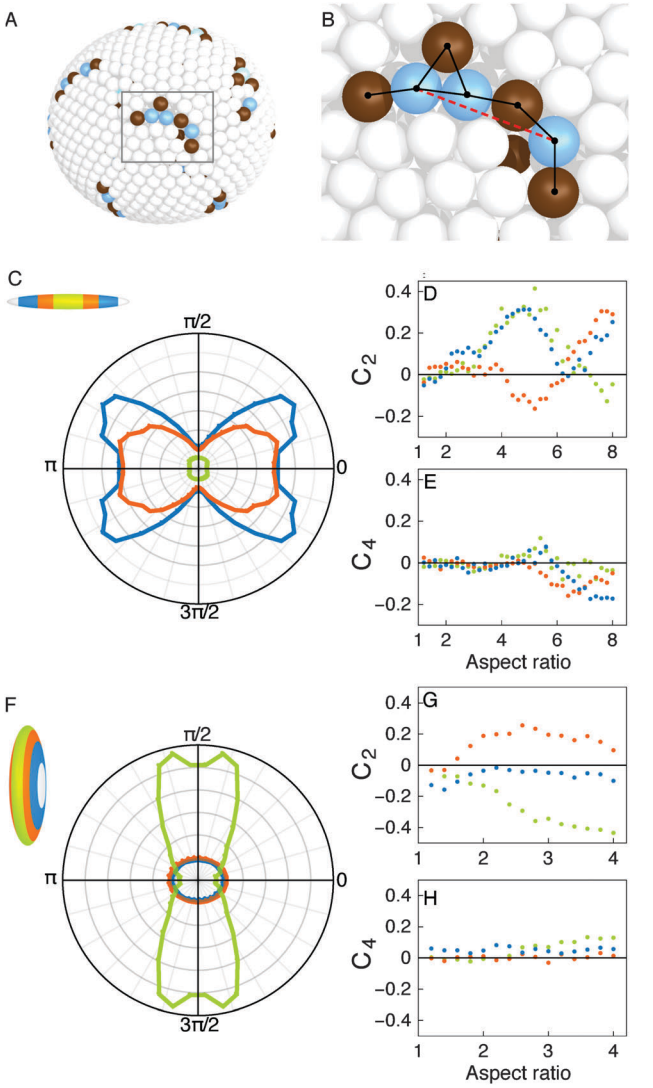

Fig. 3 Orientation of the scars relative to the curvature anisotropy. (A) A configuration with a typical scar. (B) Close-up of the scar. Black lines show edges in a graph comprising the scar. The red dashed line shows a chain of length 3. Results are shown for (C–E) prolate and (F–H) oblate ellipsoids. The C_2 (D, G) and C_4 (E, H) order parameters for prolate and oblate ellipsoids, respectively, are plotted as a function of aspect ratio for different regions along the symmetry axis of the ellipsoid: green corresponds to the center, orange to the mid-region, and blue to the ends. (C) and (F) show the ODF of chains in the center, mid-regions, and ends of the ellipsoid, respectively, for prolate ellipsoids of aspect ratio 8 in (C) and oblate ellipsoids of aspect ratio 4 in (F). Insets of (C) and (F) illustrate the regions used for spatial binning.

with $\vec{t}_\theta$ is recorded as the orientation of the chain. The z-component of the midpoint of each chain is recorded as its position and is used to examine how the coupling varies across the surface.

The analysis was applied to an ensemble of simulation results as follows: for a given aspect ratio, the orientations of all chains of length l are collected across simulations with $N \in [710, 800]$ in increments of $\Delta N = 10$ (with 50 results at each N resulting in 500 simulations). Order parameters C_2 and C_4 are then calculated from this ensemble. Because the curvature anisotropy varies with the z-coordinate along the surface, results can be divided according to their position. In our analysis, we exclude scars in the regions near the poles which make up 10% of the surface area as here the curvature tensor is degenerate and the alignment is undefined. The rest of the surface is broken into six equal-area, azimuthally symmetric regions, as illustrated in the insets of Fig. 3C and F, and data from symmetric regions on opposite halves of the ellipsoid are combined. A chain length of $l = 3$ was used as this is long enough to capture scar behavior while having enough chains for statistical purposes. Shorter chain lengths show a weaker tendency to orient.

The behavior exhibited by prolate ellipsoids is rather complicated, as seen in the plots of order parameter *versus* aspect ratio in Fig. 3D and E. In the center region near the equator, scars are nematic along the $\vec{t}_\theta$ direction between aspect ratio 3.6 and 6. At higher aspect ratio this center region is very flat, leading to fewer scars, and so any orientational order is insignificant. In the mid-regions between the equator and poles, scars become nematic along the $\vec{t}_\phi$ direction at aspect ratio 4.4, and then transition to nematic along the $\vec{t}_\theta$ direction at aspect ratio 6.4. Scars near the poles show nematic order along $\vec{t}_\theta$ above aspect ratio 2, although this order peaks near aspect ratio 5, then drops to $C_2 = 0$ at aspect ratio 6.4 before increasing again. Interestingly, scars on highly prolate ellipsoids can also show C_4 order. This appears in the mid regions above aspect ratio 5.2, and in the end regions above aspect ratio 6.

The chain ODFs for prolate ellipsoids of aspect ratio $a = 8$ in Fig. 3C illustrate the trends that appear at high aspect ratio. It is apparent from the green curve that that there are few chains in the relatively flat center of the ellipsoid. The orange curve shows a high degree of nematic order directed along the polar direction in the mid-region, and the blue curve for the ends shows nematic order along the polar direction, as well as a peak between the directions of principal curvature, which is indicative of negative C_4 order.

The case of scar orientation on oblate ellipsoids is more straightforward. The order parameters are plotted as a function of aspect ratio for different azimuthally symmetric regions across the surface, in Fig. 3G and H. Scars at the equator exhibit a high degree of nematic order in the $\vec{t}_\phi$ direction, which increases linearly with aspect ratio up to $a = 4$. This is unsurprising, because the curvature on highly oblate ellipsoids is localized to a nearly one-dimensional region around the equator of the ellipsoid, and so one expects the scars to form there, aligned along the equator. There is also a small degree of C_4 ordering. In the regions midway between the equator and poles, there is a weak coupling of scars along the $\vec{t}_\theta$ direction. These trends are illustrated for $a = 4$ in Fig. 3F the green curve for the edges displays a peak near the azimuthal direction, whereas the orange and blue curves show that there are fewer chains without much order in the flatter regions.

While the scar orientation results for the oblate case are easily understood, the ordering of the scar orientation on prolate ellipsoids is far more complicated. The orientation varies greatly depending on chain position and ellipsoid aspect ratio. Especially surprising is the emergence of C_4 ordering, which corresponds to a tendency for chains to align in a direction intermediate to the directions of principal curvatures.

2.3 Scar transition

As is well known from previous work,[14,16] packings of spheres on spherical surfaces exhibit a transition: for low particle numbers, only the twelve defects required by topology are present; above a critical particle number N_c, it is favorable for larger defect structures to occur, typically chains of scars extending from a core disclination. Increasing N above N_c leads to a monotonic increase in average scar length.

From our simulation results of packings with $10 < N < 800$, we calculated the average number of excess dislocations per topologically required disclination for each (a, N). Defects were weighted in the analysis by the absolute value of their charge. Given that there are two disclinations per dislocation, and 12 core disclinations, the number of excess dislocations per scar is calculated thus,

$$n_d = \frac{1}{2}\left(\frac{\sum_i |q_i|}{12} - 1\right), \quad (6)$$

where the sum is taken over all defects. This quantity captures the same information as the scar length but is easier to calculate, as individual scars are often not well defined.

Results of the analysis are displayed in Fig. 4. Prolate ellipsoids [Fig. 4A] show the experimentally observed behavior for low aspect ratio: for $N < 100$ particles there are few excess defects, but at higher particle numbers there is a roughly linear increase in the

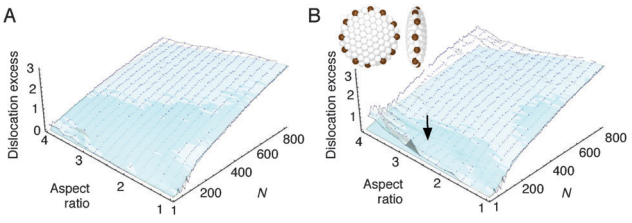

Fig. 4 The number of excess dislocation defects per scar on (A) prolate ellipsoids and (B) oblate ellipsoids. Points and white surface represent the simulation data. The blue surface represents the prediction of the model in eqn (7). For low aspect ratio near 1, there is a clear scar transition, which is not present at aspect ratios far from 1. The inset in (B) shows a highly commensurate oblate packing with $N = 140$ and $a = 2.6$. Note that data for oblate ellipsoids with $N = 10$, $a \geq 2.0$ and $N = 20$, $a \geq 3.0$ has been excluded.

number of excess defects. As aspect ratio increases, however, the transition is softened such that there is a smooth increase in excess defects with N. This is reminiscent of how applied fields soften phase transitions;[29] here the anisotropy of the curvature seems to play a similar role.

The oblate packings show the same trends [Fig. 4B]. There is, however, an additional feature that stands out. At $N = 140$, $a > 2$, there is a set of nearly scar-free configurations. This is due to commensurability as the particle number and surface geometry for these cases are compatible with a highly symmetric packing with only the minimally required defects, as seen in the inset of Fig. 4B. Similar commensurability issues occur in other systems, *e.g.* sphere packings on cylinders.[30]

The model for defect number density developed above in the defect distribution subsection can be applied to predict the average scar length for a given aspect ratio and particle number. For each point in our parameter space, we integrate eqn (4), estimating r by assuming a packing fraction of $\phi = 0.86$ (see eqn (8) below). Our result for scar length is given by,

$$n_{\mathrm{d}} = \frac{1}{2}\left(\frac{\int \rho_{\mathrm{n}} \mathrm{d}A}{12} - 1\right). \quad (7)$$

The results are plotted in Fig. 4A and B, alongside the simulation data. For prolate ellipsoids, we see excellent agreement. Perhaps most importantly, the scar transition is softened at high aspect ratios, as in the simulation results. For oblate ellipsoids, the model does not fit the simulation results quite as well; it tends to underpredict the scar length, especially at higher aspect ratio. It does, however, exhibit softening of the scar transition.

A striking difference between these results and those from a previous study is that here, for hard particles, the transition occurs at a lower particle number; in ref. 16 it was seen at $N_{\mathrm{c}} \approx 400$ using colloidal particles with a soft repulsive interaction. We therefore performed simulations (see Methods) using two different potentials, $V = d^{-1}$ and $V = d^{-6}$ (where d is the interparticle separation), the results of which are shown in Fig. 5. For soft particle packings, we take the average scar length of the five lowest energy configurations obtained out of an ensemble of 50. For the hard spheres, $N_{\mathrm{c}} \approx 80$, while for the two soft potentials the transition occurs around $N_{\mathrm{c}} \approx 200$ (which appears to be within the uncertainty of the result presented in ref. 16). The defect number increases at the same rate with respect to particle number for both soft potentials. This supports the conclusion in ref. 16 that, for soft particles, the scar transition does not depend on the specific form of the particle potential. For hard particles we have quantitatively different behavior. Visual inspection of hard and soft sphere configurations reveals that hard sphere configurations possess gaps (Fig. 5A). It is rare to find a lone disclination; it is much more common to find a disclination attached to one dislocation (*i.e.* a small 5–7–5 scar) adjacent to a gap in the packing. This isn't seen in soft particle configurations (Fig. 5B), as the energy penalty is too high, rather a particle can be squeezed to fill in the gaps. The fact that hard particle packings tend to have gaps makes them especially suitable for chemical functionalization as described in ref. 5.

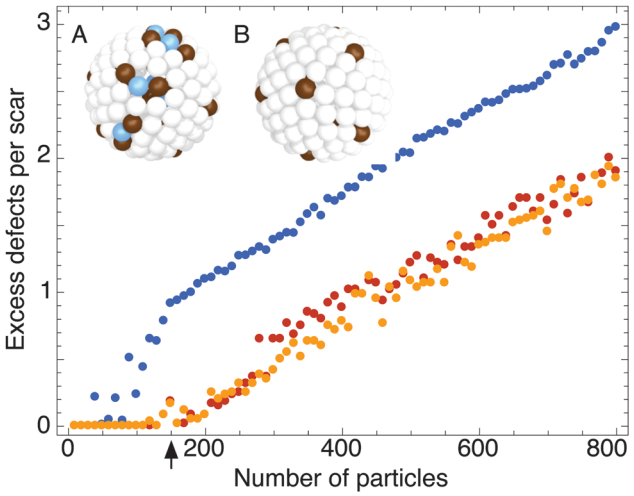

Fig. 5 Excess dislocations per scar as a function of particle number for hard (blue) and soft $V = 1/d$ (orange) and $V = 1/d^6$ (red) interactions. Inset (A) is a hard particle packing and inset (B) is a soft particle packing. The arrow indicates the particle number of the inset packings.

2.4 Packing fraction and symmetry

We now turn to how the packing fraction varies with respect to particle number and ellipsoid aspect ratio. To simplify the calculation we make the approximation, valid for large N, that the area covered by a particle is its projection onto a flat 2D surface,

$$\phi = \frac{N\pi r^2}{A}, \quad (8)$$

where A is the area of the underlying surface. We checked the validity of this estimate by numerically integrating the area of intersection between the surface and the spheres on oblate surfaces of aspect ratio 4.0, and found that the difference between our estimate and the true value is very small: using the projected area underestimates the packing fraction by approximately 1% for packings with $N = 100$ and 0.1% for packings with $N = 800$.

For large N, the packing fraction increases slightly with aspect ratio. This is because for large a the curvature—and hence the defects—are mainly localized to the poles on prolate surfaces or the equator on oblate surfaces and so more of the surface can be covered by the planar hexagonal packing, consistent with the results of the above subsections on the defect distribution and scar transition. For low N, the opposite tends to be true; the packing fraction decreases with aspect ratio. However, the trend is more complex and the packing fraction is sensitive to both N and a at low N. Visual inspection of these configurations reveals that for specific combinations of N and a, the packings have a high degree of symmetry, suggesting a commensurability effect, such as that seen in the scar transition subsection above.

To identify these commensurate combinations, we conducted a more thorough search for symmetric packings using the second data set. An arbitrary packing must break the ellipsoidal symmetry group of the surface and hence must belong to some finite subgroup of $D_{\infty h}$; most packings at high particle number do so trivially, retaining only the identity element. Defining a suitable inner product (A, B) that measures the distance between two packings, a packing possesses a symmetry $\mathscr{C}$ if $(A, \mathscr{C}A) = 0$ where $\mathscr{C}$ is a group element of $D_{\infty h}$. The elements $\mathscr{C}$ can be constructed from the group generators: (i) an infinitesimal rotation about the ellipsoid symmetry axis; (ii) spatial inversion, and (iii) a rotation by π about an axis perpendicular to the symmetry axis.

We used a norm (A, B) defined such that,

$$(A,B) = \sqrt{\frac{1}{N}\sum_{i}^{N}\left(\frac{\min_j\left|\vec{a}_i - \vec{b}_j\right|}{r}\right)^2}, \qquad (9)$$

where the $\vec{a}_i$ and $\vec{b}_j$ are the positions of particles in packings A and B, respectively: for each particle in A, the closest particle in B is found and the separations between these pairs are divided by the particle radius. The root mean square of these normalized separations is then taken as the inner product. From this, together with the group generators, all symmetries such that $(A, \mathscr{C}A) \leq \varepsilon$, a threshold separation were found. From this catalog of symmetries, for a particular configuration the appropriate group was determined. From a collection of configurations with a given (N, a), the most symmetric configuration was chosen by the following procedure. First, the configurations with the largest symmetry group were identified. Then, for each of these configurations, the symmetry group element with the highest symmetry norm was identified. Finally, the configuration with the minimum highest symmetry norm was chosen as the most symmetric.

The results of this analysis are displayed in Fig. 6A showing the order and chirality of the symmetry group of the best packing for each combination of particle number and aspect ratio. The degree of rotational symmetry for each packing is shown in Fig. 6F. One striking feature is that, for certain particle numbers, long vertical stripes appear in the plots representing commensurate aspect ratios for that particle number. Furthermore, low N favors achiral packing while chiral packings occur more often for higher particle number. For prolates the stripes occupy a narrow range of aspect ratio and occur in band-like sequences described by a straight line $a = mN$ with slope m. Each of these sequences corresponds to a different degree of rotational symmetry n_r, and the particle numbers in the sequence are separated by n_r. Inspecting the configurations in a single sequence, the difference between a configuration with N particles and the next with $N + n_r$ particles is that an additional row of n_r particles has been inserted in the space created by the longer aspect ratio. This is illustrated by a sequence of configurations with fourfold rotational symmetry in Fig. 6G–J.

For oblate ellipsoids, the symmetric configurations for N particles occur at a much broader range of aspect ratios and

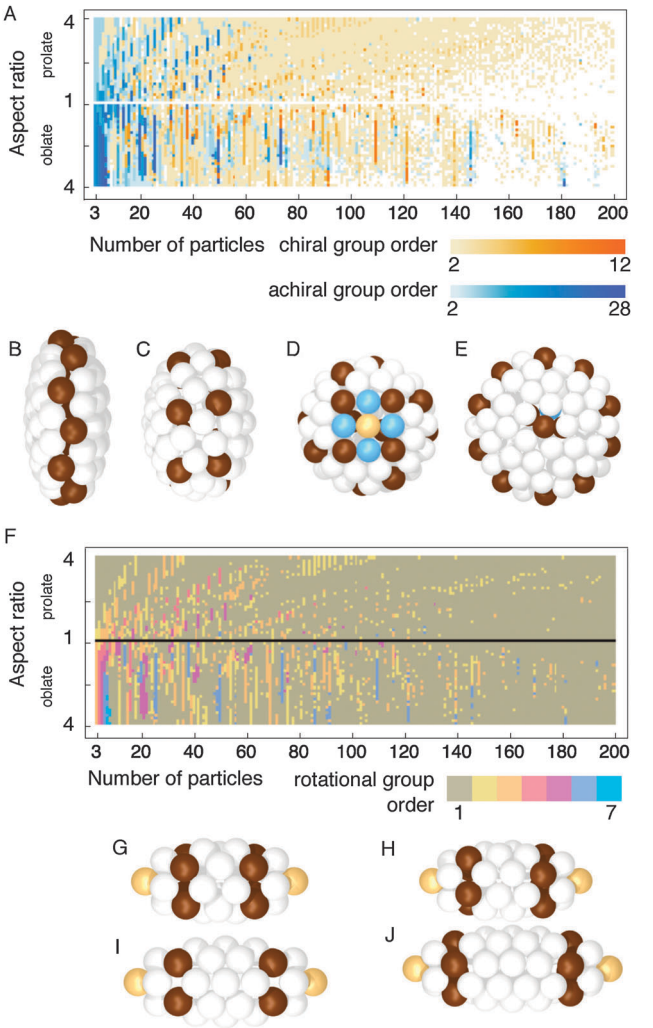

Fig. 6 The symmetry landscape for packings with varying particle number and aspect ratio, using a symmetry norm cutoff of 0.1. (A) Shows the chirality and the order of the largest symmetry group found. Orange represents chiral packings and blue represents achiral packings. The boldness of the color corresponds to the order of the packing's symmetry group as shown in the key. Note that packings whose only symmetry is the identity are colored white to distinguish them as being trivially symmetric. Sample packings are shown: (B) an achiral packing with $N = 74$, $a = 2.5$; (C) a chiral packing with $N = 74$, $a = 1.5$—note that (B) and (C) have the same particle number, but show different chirality for different aspect ratio; (D) a packing with fourfold rotational symmetry with $N = 69$, $a = 1.4$; (E) a packing with fivefold symmetry $N = 76$, $a = 2.4$. Light brown particles have $c = 4$. (F) shows the degree of rotational symmetry of each configuration about its ellipsoidal symmetry axis. Note that for both (A) and (F), no data is shown for $a = 1$ (spheres) as the spherical symmetry group is not a subgroup of $D_{\infty h}$. Sample packings are shown for (G) $N = 30$, $a = 2.4$; (H) $N = 34$, $a = 2.5$; (I) $N = 38$, $a = 2.7$; (J) $N = 46$; these packings all occur in the diagonal band of fourfold rotational symmetry in the top left of (F).

symmetric configurations are observed at much higher N and tend to have six-fold rotational symmetry. The reason for this is that the high curvature at the end of the prolate ellipsoids accommodates n_r-fold defects at the poles, and these appear to determine the rotational symmetry for the entire configuration; for oblates, the poles have low curvature and promote hexagonal

packing, hence causing six-fold rotational symmetry to be more common. Interestingly, other degrees are present including n_r = 4 and n_r = 5 and these configurations contain regions of highly oblique packings (Fig. 6D and E).

In general, these symmetric packings are notable because they contain a high degree of hexagonal ordering over much of their surface, with evenly spaced defects throughout. This high degree of regularity should provide stability to the packed structure, and reduce the likelihood of failure from irregularly spaced defects.

3 Experiment

An experimental realization of ellipsoidal arrested droplets was performed to confirm the stability of these structures. Ellipsoidal droplets with arrested interfaces are produced by preparing a Pickering emulsion and then mixing the emulsion to deform and arrest the droplets in an elongated shape. Details are given in Methods.

Fig. 7 shows several examples of the arrested droplets observed. Because the curvature of a droplet is significant across its surface, several focal planes have been combined in the images in order to study the packing of spheres on the drop surface. Particle coordinates are determined by finding the local brightness maxima in the image, recording their coordinates, and correcting for any unrealistic results *via* direct comparison with the experimental images.

Arrest is able to preserve shapes identical to intermediate states of droplets in an elongation field,[31] as seen in the Fig. 7A and C, and even shapes resembling sections of such shapes as in the case of Fig. 7E. While the dynamical formation of these shapes was not studied, it is clear that a wide range of geometries can be formed. We note that the droplet of aspect ratio 5.1 has a spherocylindrical geometry, as opposed to ellipsoidal.

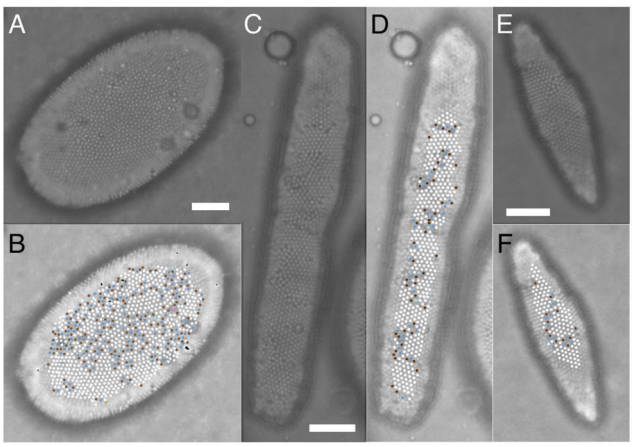

Fig. 7 Experimental data for particle-stabilized droplets of aspect ratio (A, B) 1.6, (C, D) 5.1, and (E, F) 3.0. Scale bars represent 15 μm. (A, C, E) Microscope images; (B, D, F) reconstructed particle positions, colored by coordination number as determined by Delaunay triangulation of the particle centroids—4: light brown, 5: dark brown, 6: white, 7: dark blue, 8: light blue, 9: purple. In general, defects are more common and are more likely to be found at low-curvature regions of the droplet in the experiments than in simulations.

Fig. 7B, D and F shows the results of a Delaunay triangulation of the sphere coordinates. We do not display particles at the boundary of the triangulation, as they include spurious edge defects identified as a result of the boundary rather than the ordering of the particles. In each case the arrested state of the interfacially adsorbed spheres is evident from the visible regions of crystalline order. Generally, however, the experimental droplets contain more defects than the simulated packings. In Fig. 7B a high degree of hexagonal close-packing is noted near the ends of the droplet, while the center of the structure is more disordered with a higher defect density. Three important factors present in the experiment that are not accounted for in the simulation may contribute to this. First, the evolution of the surface as it relaxes will influence particle rearrangement. Different parts of the surface will grow or shrink at varying rates, affecting where crowding first occurs. Second, particles adsorbed at an interface will not act as purely hard spheres. Capillary interactions caused by the deformation of the surface by the particles will lead to attractive interactions between particles.[25] This may lead to aggregation of particles during relaxation and is likely to influence the final ordering of the arrested state. Finally, as discussed in the introduction, the experimental relaxation does not take place quasistatically, as is posited by studying the packing limit; it is highly likely that the particles are arrested in a nonoptimal and possibly metastable glassy state.

4 Conclusion

In this paper, we show that defects in the packing of hard spheres onto an ellipsoidal surface couple nontrivially to the curvature. For low aspect ratios, the defects occur at regions of high curvature as predicted by previous studies; additional secondary peaks in the defect distribution occur in less-curved regions for prolate ellipsoids of sufficiently high aspect ratio. As previously observed for packings on a spherical surface, above a critical particle number the defects take the form of chains or ''scars'' rather than isolated defects. This scar transition occurs at a lower particle number than the previously studied case for soft interparticle interactions, and is softened by the presence of anisotropic curvature. The alignment of the scars with the curvature is more complicated: in flat regions, there is no alignment; in intermediate regions, there is weak uniaxial alignment with the minimum curvature; in regions of strong curvature, quadrupolar alignment is seen. We identified a rich catalog of symmetric configurations from our simulations, each belonging to a subgroup of the ellipsoidal symmetry group. Plotting the subgroup order in (N, a) space reveals commensurate surfaces that promote symmetric packings. Finally, we were able to use the mechanism of arrest to sculpt ellipsoidal Pickering emulsion droplets of varying aspect ratio, demonstrating the validity of the fundamental idea. While careful analysis of these experimental packings reveals scars as predicted, the defects appear to agglomerate in regions other than those of strongest curvature, suggesting that dynamical effects play a significant role in the ordering as well as the geometric effects studied here.

Heuristic models of geometrically frustrated order are able to explain some of the observed features—namely the defect charge density and average scar length for prolate ellipsoids, and the softening of the scar transition. These models fail, however, to capture features such as the secondary peak in the defect number density on prolate ellipsoids, and they break down for highly oblate ellipsoids.

One question raised by this work is how these non-equilibrium systems of arrested hard spheres compare to equilibrium curved membranes in the continuum limit. Most clearly, the hard-particle interaction influences the scar transition. The non-trivial nature of the results presented in the defect distribution and scar orientation sections is evidence of a complicated coupling between order and curvature. Whether this coupling is consistent with eqn (1) and (2) is an open question.

The role of dynamical effects on ordering is also unclear at this time. As outlined above, possible influences include the varying rate of area change across the droplet, inter-particle interactions, and rate of the droplet shape relaxation. A study of the role of these dynamical influences on the order is in preparation.

Methods

Experimental preparation of arrested droplets

Emulsions are first prepared by mixing 3% w/w monodisperse 1.5 μm diameter precipitated silica particles (Nippon-Shokubai KE-P150) into hexadecane (Sigma-Aldrich, 99%).[9] A volume of the silica-hexadecane dispersion is then emulsified into an equal volume of deionized water by manual shaking for three minutes. The emulsion was then aged for 24 hours and inspection revealed a small fraction of elongated droplets. Imaging of the droplets is carried out on a Leica DM2500M light microscope using phase contrast optics.

Hard-sphere simulations

We employ a stochastic inflation packing algorithm inspired by the Lubachevsky–Stillinger algorithm, which is known to yield packings of high coverage fraction.[32] In each packing simulation, a fixed ellipsoidal surface, either prolate or oblate, is chosen with aspect ratio a and the length of the semi-minor axis is fixed to be unity in dimensionless units. Particles are modeled as monodisperse hard spheres of radius r that is slowly increased during the simulation. The number of particles N is specified and particles are deposited at the start of the simulation by random sequential adsorption such that the center of each particle is constrained to lie on the surface of the ellipsoid. Initially, r is such that the packing fraction is $\phi = 0.05$.

The algorithm proceeds by two kinds of moves: (i) Monte Carlo diffusion steps where particles are moved randomly along the surface and (ii) inflation steps where the radius of all particles is increased by δr. In each diffusion step, N individual Monte Carlo moves of randomly chosen particles are attempted. The step size is chosen randomly using a Gaussian distribution, as described below. Only moves that do not result in overlap are accepted, with overlaps checked for in the 3D configuration frame.

The moves are performed in the 2D space of conformal surface parameters (u, v), hence yielding a radially symmetric probability distribution of moving a certain arclength s in any tangential direction from the current location. The surface is parametrized as,

$$x(\theta, \phi) = (x_0 \sin\theta\cos\phi,\ x_0 \sin\theta\ \sin\phi,\ z_0\cos\theta), \quad (10)$$

where $x_0 = 1$, $z_0 = a$ for prolate surfaces and $x_0 = a$, $z_0 = 1$ for oblate surfaces. The determinant of the metric is,

$$g(\theta) = \frac{1}{2}x_0 \sin(\theta)^2\left(z_0{}^2 + x_0{}^2 + \left(z_0{}^2 - x_0{}^2\right)\cos(2\theta)\right), \quad (11)$$

and the conformal parameter u is given by the integral of the conformal factor,

$$u(\theta) = \int_{\pi/2}^{\theta} \sqrt{g(\theta')}\mathrm{d}\theta', \quad (12)$$

which can be inverted to find $\theta(u)$. We do an approximate inversion by calculating $u(\theta)$ for values of θ from 0 to π in increments of π/100 and using a high order polynomial least squares fit on these points, enforcing equality between the fit and exact values at the endpoints $\theta = 0$ and $\theta = \pi$. The conformal coordinate v is simply $v(\phi) = \phi$.

Given the definitions above, diffusion steps are taken as follows. An unscaled step size is chosen for each direction, Δu_0 and Δv_0, from a normal distribution with variance 1. These are scaled by the simulation step size σ and by the inverse of the conformal factor to give step sizes in the (u, v) conformal space:

$$\Delta u = \frac{\sigma \Delta u_0}{\sqrt{g(\theta(u))}} \quad (13)$$

$$\Delta v = \frac{\sigma \Delta v_0}{\sqrt{g(\theta(u))}}. \quad (14)$$

These steps are used to update the previous u and v coordinates of the particle, which are then transformed to the θ and ϕ coordinates as explained above. Finally, the surface parametrization eqn (10) is used give the particle coordinates in the 3D configuration space.

Because θ must have a value between 0 and π, we take the following step if it falls outside this range at any point. If u is greater than $u(0)$ (less than $u(\pi)$), we set $u = 2u(0) - u$ ($u = 2u(\pi) - u$) and $v = \mathrm{mod}(v + \pi, 2\pi)$, *i.e.* we allow the particle to pass over the coordinate singularity at the poles of the surface.

As the particles diffuse, σ is varied in order to more efficiently explore relevant areas of configuration space (leading to large steps when the configuration is loosely packed and smaller, more relevant steps when tightly packed.) The initial value of σ scales with the square root of the ellipsoid surface area A, $\sigma_{\mathrm{init}} = 1 \times 10^{-4}\sqrt{\frac{A}{4\pi}}$. After each time step, the fraction of attempted moves that were accepted is calculated. The length scale σ is then decreased by 1% if the acceptance fraction is <0.5 and increased by 1% otherwise; σ is reset after each

inflation (described below) to its initial value. Bounds are imposed such that $1 \times 10^{-6} < \sigma < 1$. Adjusting σ leads to improved performance of the algorithm as the particles can diffuse more when they are less densely packed and take smaller steps (which are more likely to be accepted) when they are more densely packed. We do this as it is known that adaptive algorithms lead to packings of higher density.[33] We emphasize that in this work the Monte Carlo approach is used as an optimization strategy; it is not intended to, and indeed cannot, replicate the physical process by which the structures form since the σ updates are non-Markovian.

After $M = 100$ diffusion steps, an inflation step is performed where the particle radius is increased slightly ("inflated") either by a specified fixed amount $\Delta r = 1 \times 10^{-5}\sqrt{\frac{A}{4\pi}}$ or by the half of the largest amount allowed that would not result in the overlap of any pair of particles, whichever is smaller.

The halting criteria for these simulations is as follows: every $L = 100$ inflation steps, the relative change in coverage fraction $\Delta\phi$ is calculated. If this is less than a specified value $\Delta\phi_{\text{tol}} = 10^{-4}$ then the simulation halts.

Soft particle simulations

In order to compare our results regarding scar formation in hard particle packings to other work involving particles with soft interactions, we performed a set of simulations using a modified Monte Carlo algorithm which incorporates a soft interparticle potential. In order to test potentials of different softness, the interparticle potentials are set as either $U_{\text{int}} = d^{-1}$ or $U_{\text{int}} = d^{-6}$ (where d is the center-to-center distance between particles). The particles diffuse similarly to the hard particle simulation with two differences: the average step size σ is constant for all moves, and moves are accepted or rejected using a Metropolis scheme,[34] with acceptance probability

$$P = \begin{cases} 1 & \Delta U < 0 \\ \exp(-\Delta U/k_{\text{B}}T) & \Delta U > 0 \end{cases} \quad (15)$$

where ΔU is the change in the system energy after a single particle move. The initial temperature is set by using a rough estimate of what the energy of a single particle in the final configuration will be assuming six-fold ordering and that nearest neighbor interactions dominate: $T_0 = 6U_{\text{int}}(2r_{\text{est}})/k_{\text{B}}$, where $r_{\text{est}} = \sqrt{A/N}$ is an estimate of the average particle separation. The system is annealed by multiplying the temperature by 0.99 after every 100 sets of diffusion moves until $\exp(-\Delta U/k_{\text{B}}T) \to 1$ within machine precision. After every 100 sets of diffusion moves, the change in energy is recorded and the simulation halts once this change in energy is less than 1×10^{-16}.

Defect analysis of simulations

To analyze defects in the simulated configurations, we use a ball-pivoting algorithm[35] in the mesh-generation software Meshlab to generate triangulations of the particle centroids. These triangles are then equiangulated by a custom script to remove narrow triangles. Edges are flipped in random order and accepted if they improve the triangulation; this is repeated until a full sweep of the mesh yields no further improvements. From these optimized triangulations, the coordination number of each particle is given by the number of particles to which it is connected.

Acknowledgements

TJA and CJB were funded by a Tufts International Research grant to conduct part of this research at UNSW Australia. CJB was partly funded by a Tufts Collaborates! and a Tufts Innovates! grant. ZW was funded by a UNSW Faculty of Engineering Taste of Research Summer Scholarship. We would like to thank Marco Caggioni (Procter & Gamble Co.) for fruitful discussions about emulsion arrest.

References

1 T. H. Weiss, A. L. Mills, G. M. Hornberger and J. S. Herman, *Environ. Sci. Technol.*, 1995, **29**, 1737–1740.
2 J. A. Champion and S. Mitragotri, *Proc. Natl. Acad. Sci. U. S. A.*, 2006, **103**, 4930–4934.
3 S. E. A. Gratton, P. A. Ropp, P. D. Pohlhaus, J. C. Luft, V. J. Madden, M. E. Napier and J. M. DeSimone, *Proc. Natl. Acad. Sci. U. S. A.*, 2008, **105**, 11613–11618.
4 A. Donev, I. Cisse, D. Sachs, E. A. Variano, F. H. Stillinger, R. Connelly, S. Torquato and P. Chaikin, *Science*, 2004, **303**, 990–993.
5 D. R. Nelson, *Nano Lett.*, 2002, **2**, 1125–1129.
6 S. U. Pickering, *J. Chem. Soc.*, 1907, **91**, 2001–2021.
7 B. P. Binks, *Curr. Opin. Colloid Interface Sci.*, 2002, **7**, 21–41.
8 M. Cui, T. Emrick and T. Russell, *Science*, 2013, **342**, 460–463.
9 A. B. Pawar, M. Caggioni, R. Ergun, R. W. Hartel and P. T. Spicer, *Soft Matter*, 2011, **7**, 7710–7716.
10 H.-L. Cheng and S. S. Velankar, *Langmuir*, 2009, **25**, 4412–4420.
11 A. Dinsmore, M. F. Hsu, M. Nikolaides, M. Marquez, A. Bausch and D. Weitz, *Science*, 2002, **298**, 1006–1009.
12 H. Seung and D. Nelson, *Phys. Rev. A: At., Mol., Opt. Phys.*, 1988, **38**, 1005–1018.
13 A. Pérez-Garrido, M. Dodgson and M. Moore, *Phys. Rev. B: Condens. Matter Mater. Phys.*, 1997, **56**, 3640–3643.
14 M. Bowick, D. Nelson and A. Travesset, *Phys. Rev. B: Condens. Matter Mater. Phys.*, 2000, **62**, 8738–8751.
15 M. Bowick and A. Travesset, *J. Phys. A: Math. Gen.*, 2001, **34**, 1535–1548.
16 A. Bausch, M. Bowick, A. Cacciuto, A. Dinsmore, M. Hsu, D. Nelson, M. Nikolaides, A. Travesset and D. Weitz, *Science*, 2003, **299**, 1716–1718.
17 T. Einert, P. Lipowsky, J. Schilling, M. J. Bowick and A. R. Bausch, *Langmuir*, 2005, **21**, 12076–12079.
18 V. Vitelli, J. Lucks and D. Nelson, *Proc. Natl. Acad. Sci. U. S. A.*, 2006, **103**, 12323–12328.

19 L. Giomi and M. Bowick, *Phys. Rev. B: Condens. Matter Mater. Phys.*, 2007, **76**, 054106.
20 L. Giomi and M. Bowick, *Phys. Rev. E: Stat., Nonlinear, Soft Matter Phys.*, 2008, **78**, 010601.
21 W. T. M. Irvine, V. Vitelli and P. M. Chaikin, *Nature*, 2010, **468**, 947–951.
22 E. Bendito, M. J. Bowick, A. Medina and Z. Yao, *Phys. Rev. E: Stat., Nonlinear, Soft Matter Phys.*, 2013, **88**, 012405.
23 P. Hilton and J. Pedersen, *Am. Math. Mon.*, 1996, **103**, 121–131.
24 S. Torquato and F. H. Stillinger, *Rev. Mod. Phys.*, 2010, **82**, 2633–2672.
25 P. A. Kralchevsky and K. Nagayama, *Adv. Colloid Interface Sci.*, 2000, **85**, 145–192.
26 W. Roos, R. Bruinsma and G. Wuite, *Nat. Phys.*, 2010, **6**, 733–743.
27 V. N. Manoharan, M. T. Elsesser and D. J. Pine, *Science*, 2003, **301**, 483–487.
28 A. Azadi and G. M. Grason, *Phys. Rev. Lett.*, 2014, **112**, 225502.
29 L. D. Landau and E. M. Lifshitz, *Statistical Physics*, Butterworth-Heinemann, 1980.
30 D. Wood, C. Santangelo and A. Dinsmore, *Soft Matter*, 2013, **9**, 10016–10024.
31 M. Tjahjadi, J. M. Ottino and H. A. Stone, *AIChE J.*, 1994, **40**, 385–394.
32 B. Lubachevsky and F. Stillinger, *J. Stat. Phys.*, 1990, **60**, 561–583.
33 S. Torquato and Y. Jiao, *Phys. Rev. E: Stat., Nonlinear, Soft Matter Phys.*, 2010, **82**, 1–14.
34 B. P. Flannery, S. Teukolsky, W. H. Press and W. T. Vetterling, *Numerical Recipes in C: The Art of Scientific Computing*, Cambridge University Press, 2007.
35 F. Bernardini, J. Mittleman, H. Rushmeier, C. Silva and G. Taubin, *IEEE Trans. Vis. Comput. Graph.*, 1999, **5**, 349–359.

